The ESO/ADONIS system: a 3 years experience in observing methods*

D. Le Mignant[1], F. Marchis[1], D. Bonaccini[1],
P. Prado[1], E. Barrios[1], R. Tighe[1], V. Merino[1], A. Sanchez[1],
the 3.60m Telescope Team and ESO adaptive optics team

[1] European Southern Observatory, Casilla 16317, Santiago 19, Chile
[2] European Southern Observatory, K. Schwarzschild St.2,, 85748 Garching, Germany
* Comments to: David.Le-Mignant@obs.ujf-grenoble.fr

Abstract – The ESO/ADONIS adaptive optics system is mounted at the Cassegrain focus of the 3.60m telescope at La Silla Observatory (Chile). We review the observational context of this AO system offering various observing modes in direct imaging as well as a set of prefocal optics including Fabry-Perot etalons and coronograph. Rather than relating the ideal observational cases, we emphasize on the observing difficulties that we have experienced in the past years with various observational schemes.

---

1 Introduction:

The ADaptive Optics Near-Infrared System (ADONIS) architecture and performances have been recently described in several papers (Beuzit et al. 1997, Bonaccini et al. 1997). ESO adaptive optics system (COME-ON+, ADONIS) have been routinely used by the ESO community since 1993. As of October 98, 33 astronomical science papers have been published in refereed journals from data collected with the ESO AO systems.
In this paper, we concentrate on the observing methods that has been carried out with ADONIS in the past three years. We analyze the AO observational context and propose a classification of the different parameters of the observations.
From our experience, we illustrate the impact on image quality, of the variability of various parameters. L' band observations of Io volcanism are given as an example of ADONIS observation specificity. We comment on the coronographic imaging and spectro-imaging mode offered with ADONIS and give an example of an original method coupling both modes.

1.1 Summary of system characteristics:

The wavefront distortions of the visible incoming light are measured using one of the two Shack-Hartmann wavefront sensors (WFS) at a maximum sampling rate of 200Hz. The analysis of the wavefront and the correction to apply on it, via a 52 actuators deformable mirror and a tip-tilt mirror, are computed using a modal optimization with digital filter gain adjustment scheme (Gendron & Léna, 1995). Two NIR camera allow imaging in the 1-5μm range. Deep imaging in 1-2.4μm range can be carried out using SHARPII+ camera built for ESO by the Max Planck Institute für Extraterrestrische Physik (Eisenhauer & Hofmann 1996). The COMIC camera (Lacombe et al. 1998) built under ESO contract by Observatoire de Grenoble and Observatoire de Paris-Meudon is optimized for L to M band. Both cameras offer a set of standard photometric broad band filter as well as narrow band filters.
Two Fabry-Perot (FP) etalons with 1000 and 2200 of resolutions give spectro-imaging capacities to the AO near infrared system. A coronographic mask might be inserted in the light path, and together with the SHARPII+ cold Lyot stop allow high contrast imaging in the vicinity of bright object.

AO system	High flux WFS (Reticon)	200Hz, up to 7^{th} mag.
	Low flux WFS (EBCCD)	25-200Hz up to 13^{th} mag.
	Deformable mirror	piezo stack 52 actuators
	Modal optimization	with digital filter gain adjustment
	"ON/OFF" chopping mirror	in the NIR channel
SHARPII+ camera	Rockwell NICMOS3 array	HgCdTe 256× 256
	Wavelength domain	1-2.4μm
	Magnification lenses	35/50/100 mas/pix
	Read-out noise	38e$^-$/pix
	Linear capacity	202 000e$^-$
	Conversion factor	9.36e$^-$/ADU
	Circular Variable Filer (CVF)	Res=60 1.4-2.4 μm
	Lim. Mag. J/H/K	20.6/20.4/19.9 mag. (point source)
	Back. Level J/H/K	16,2/14.1/12.4 magn.arcsec^{-2}
COMIC	LETI/LIR array	HgCdTe 128 × 128 (anti-blooming CCD)
	Wavelength domain	1-5μm
	Magnification lenses	35/100 mas/pix
	Read-out noise	1000e$^-$/pix
	Linear capcity	5.9 10^6e$^-$
	Conversion factor	92e$^-$/ADU
	Circular Variable Filer (CVF)	Res=120 2.5-4.5 μm
	Lim. Mag. L'/M	10.1/7.7 mag. (point source)
	Back. Level L/M	2/-0.9 magn.arcsec^{-2}
Data acquisition system	integration time	individual/sequence
	chopping	any position, any sequence
	sequences	Filter sequences; FP, CVF scans
	real time display	
Prefocal optics	Fabry-Pérot 1	Low res. 1000
	Fabry-Pérot 2	High res. 2200
	linear polarization	
	Coronographic mask	6 masks from 0.35″to 6″
		Lyot mask in the camera pupil plane
Data Reduction	**eclipse**	basic and advanced arithmetics; cube handling
		flat-field and badpix. generation, shift and add...
		ADONIS data pipelines

Table 1: Summary of the ADONIS system characteristics and capabilities

Prefocal optics and NIR camera settings are controlled by the ADOCAM data acquisition system. ADOCAM also controls observing sequences including mosaicing sequence, filter sequence, FP sequence, coronographic masks choice. ADOCAM is a key element in such a complex system and allows to fit the prefocal and NIR cameras settings according to the various possible observational schemes.

Finally, ESO has developed the **eclipse** data processing tool-box (`http://www.eso.org/eclipse/` and Devillard 1997) that provide with a large set of usual and advanced NIR data reduction recipes and with specific adaptive optics imaging and spectro-imaging commands.
Data reduction pipeline, corresponding to various observing methods, have been implemented at the telescope and have been made available for the astronomers.

The ADONIS characteristics are summarized in tab.1. For any further information on the ADONIS system, we recommend our web site `http://www.eso.org/aot/adonis/`.

2 Observing with ADONIS:

The observational scheme can be considered as observer-defined choices, as a function of the scientific rationales, of the various elements characteristics composing the entire ADONIS system, and of the atmospheric changes (background emission, turbulence characteristics, ..).
In this section, we intend to classify the different constraints and parameters involved in the ADONIS observational context. We aim at demonstrating that a clear picture of those parameters is a necessary step to best carry out the given observations at a given time, for given external conditions.

We distinguish in the following the varying external conditions, from the scientific goals and requirements, and from the ADONIS various tunable parameters.

2.1 The observation master data

Those fixed parameters are system-defined, object-defined or science-defined . They will not vary during the observations. They can be listed as:

- the instrumental characteristics of AO sub-systems, NIR cameras, prefocal optics, and acquisition system (capabilities, response time, linearity domain, optics quality, bias level, intrinsic noise level...)
- the WFS reference source characteristics: magnitude, color, morphology and multiplicity
- the NIR science target characteristics: distance to the reference, magnitude, color, proper motion, vicinity a bright object, spatial extension.
- the scientific priorities and objectives of the observations: observing wavelength, spectral resolution, linear polarimetry, spatial resolution, detectivity.

2.2 The observational conditions

We gather in a second group the external parameters of the observations that are highly or slowly time variable.

- the atmospheric turbulence parameters: r_0, τ_0, θ_0, respectively Fried spatial correlation, time correlation and angular correlation parameters.
- local turbulence effects due to telescope building and dome environment, to convective air cells close to the mirrors,...
- the sky emission and absorption
- the instrumental background emission
- the zenith distance that induces thicker atmospheric layers to pass through and instrument flexure.

2.3 The tunable parameters

The considered parameters are those that can be tuned given the constraints of the two first groups. They represent levers of different kinds that can be handle by the observer to best observe.

- For the adaptive optics system:
  - the choice of the WFS
  - the WFS temporal bandwidth (for the low flux WFS case)
  - the incoming flux on the WFS sub-apertures (to adjust the PSF calibrator flux)
  - the gain optimization (mainly for faint stars)
  - the IR channel static aberration correction
  - the numerical windowing of WFS sub-apertures to reduce the light contamination from any source in the close vicinity
- For the SHARPII+ or COMIC NIR camera:
  - the individual integration time
  - the image magnification that determines the spatial sampling and the field of view (FOV).
  - the narrow or broad band filter
- For the ADOCAM data acquisition system

- the way to acquire the background emission
  * by means of "ON/OFF" ADONIS M6 mirror (choice of the *chopping* mode and frequency). Different modes are available between double or triple chopping with user-defined ON and OFF positions.
  * by giving an offset to the telescope: *staring* mode or by combining with chopping: *nodding* mode.
  * by derivation of the median background level over several "ON/OFF" positions. If inter-distances are shorter than the FOV: *on-chip-scanning* mode or *mosaicing* mode in the opposite case.
- the settings of integration sequences: number of images per "ON/OFF" position, number of "ON/OFF" positioning sequences to repeat.
- the settings of the filter, CVF scans, FP scans or polarizer scans, and the priority among them.

• For the prefocal optics:

- the choice of the K band FP spectral resolution (~1000 or ~2200)
- the choice of the coronograph mask size (between 0.35″ and 6″)
- the possibility to use the atmospheric dispersion compensator for J band observations.

2.4 Starting observing

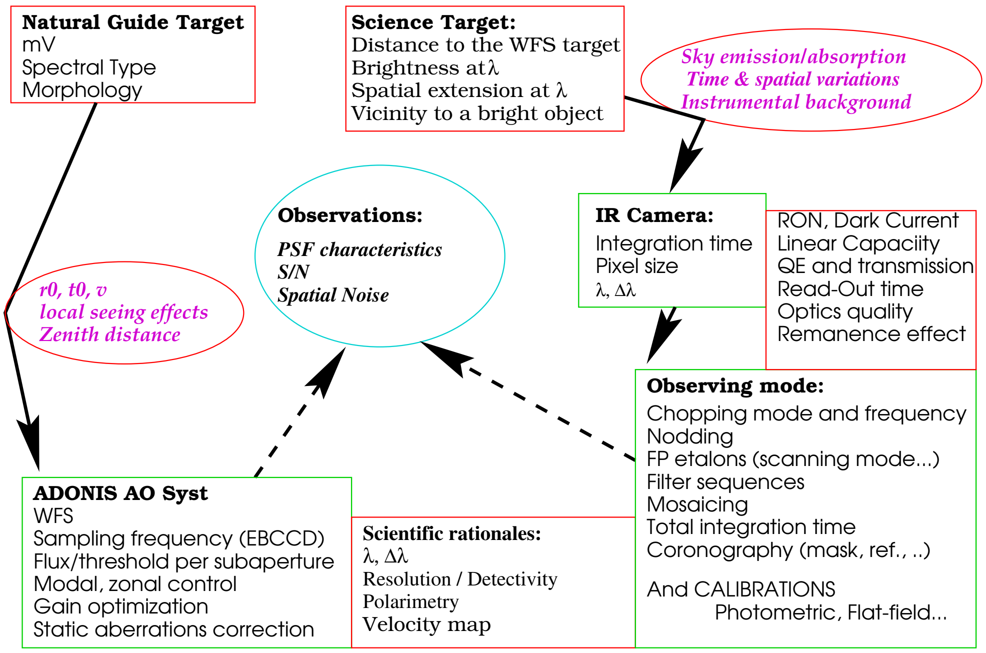

Figure 1: Schematic representation of the ADONIS observational context. The left part of the diagram deals with the AO system tunings, and the right side with the NIR cameras and data acquisition system.

Figure 1 gives a representation of the observational context. The left part of the diagram deals with the AO system tunings, and the right side with the NIR cameras and data acquisition system.
The final achievement in image quality given by the PSF characteristics, the signal to noise ratio (SNR) per pixel and the spatial noise in the final frame is given as a function of the presented parameters.
It is not expected from the observer to have in mind the all ADONIS observational context, but it is one of the support astronomer objectives to provide the astronomer with the observational context of the given observations.

In the next sections, we intend to give a concrete picture of the various varying parameters to be taken into account when observing with ADONIS.

3 Direct imaging with ADONIS:

Direct imaging with ADONIS is defined as imaging without prefocal optics. It can be either carried out with SHARPII+ or COMIC camera.
The SHARPII+ camera is optimized for 1-2.4μm range observations, and COMIC camera for the 3-5μm range.

3.1 Dominant noise in individual images

The SNR per pixel in an individual integration of t_i is given by the ratio of the source signal, to the quadratic sum of the noise contributions (Read-Out Noise, dark current, background photon noise, electronic correlated noise).
When the RON is the dominant noise, then SNR increases $\propto t_i$ in a single frame and the total SNR over N frames will be $\propto \sqrt{N} \times t_i$. Thus it is very important to increase the individual integration time up to the limit of external variations (PSF variation, background emission variation, ...).
When the background photon flux per pixel is becoming higher than RON^2, then the detector is working under BLIP (Background Limited Infrared Performances) conditions and we define the corresponding time t_{BLIP}. The SNR increases $\propto \sqrt{t_i}$ ($t_i \geq t_{BLIP}$) in a single frame, and the SNR in a final image of N frames of t_i will be equivalent to a single frame of $N \times t_i$. Once under BLIP conditions, the detector performances are no longer affected by the RON value.

From sky measurements, we have derived a median level for background emission under relatively good conditions (air humidity of 20%). Given the RON, dark current and background photon noise flux, we have computed the t_{BLIP} for SHARPII+ and COMIC (cf table 2). Due to the relatively good atmospheric conditions that we had

Camera	Band	Background emission in $e^-.s^{-1}.arcsec^{-2}$	t_{BLIP} (sec.) 100mas/pix	t_{BLIP} (sec.) 50 mas/pix
SHARPII+	J	200	650	2500
SHARPII+	H	1250	100	410
SHARPII+	SK	5000	25	105
SHARPII+	K	5600	20	90
COMIC	Lprime	$6.95\,10^7$	1.43	–
COMIC	M	$2.79\,10^8$	0.360	–

Table 2: Indicative t_{BLIP} values for SHARPII+ and COMIC in the routinely used broad band filters

during our tests, one should consider those numbers as indicative superior limits for t_{BLIP}.
It comes out of the values presented in tab 2 that J band and H band (50 mas/pixel scale) SHARPII+ observations is always limited by the RON contribution in the context of AO observations (see below for the other limitation for the integration time). For any other observation with SHARPII+, the dominant noise in the frames depends on the star brightness. The brighter the star, the higher the RON contribution.
As a reference, a 10^{th} magnitude star fills the SHARPII+ linear capacity (21 500 ADU) in 25seconds in SK band.
For COMIC 3-5μm range observations, the background photon noise is very high at those wavelength (see also Le Mignant et al., these proceedings), and the observations are always carried out under BLIP conditions.

3.2 Degradation of signal to noise

The signal to noise value in the final reduced frame (basically, after sky subtraction, flat-field correction, re-centering and average) is affected by the following variations:

- background emission time variations
- background emission spatial inhomogeneities
- PSF variations

- remanence effect
- low frequency electronic spatial noise

3.2.1 Background emission incertitudes

If the background emission (sky and instrument) is varying along the frames, it induces an uniform offset in the final image background if this variation is spatially uniform. In case of inhomogeneous background emission coming either from the sky or from the telescope, there is an additional low frequency spatial noise.

The background emission stability time-scale that we infer from our experience, are for J, H, K, L, and M broad band respectively 10 min, 6 min, 4 min, 10 sec and 2 sec. We recommend not to over-pass those value between object frame and sky frame.

In the ADONIS case, we note inhomogeneous instrumental background emission as a function of the "ON-OFF" position. The larger the observing wavelength, the higher the intensity of the background emission spatial variations. Background emission frames should be recorded in *staring* mode when observing sources fainter than the background emission in J, H, and K band.
The case of 3-5μm range observations is more complex. First, due to the sky variation time-scale ($\leq$ 10 sec) in this range, one has to observe using a *nodding* method. Secondly, there is still a remaining noise affecting the images. This remaining noise is attributed to the blurring effect of adaptive optics system on background emission (see H. Geoffray, "Thermal background blurring with ADONIS", these proceedings).

3.2.2 Flat-field estimation

Studying the SHARPII+ camera pixel response map (taking into account all the optics, from the camera to the telescope) among various filters and conditions, we derived the following conclusion:

- The standard deviation across the pixel response map is less than 5% (see figure 2).

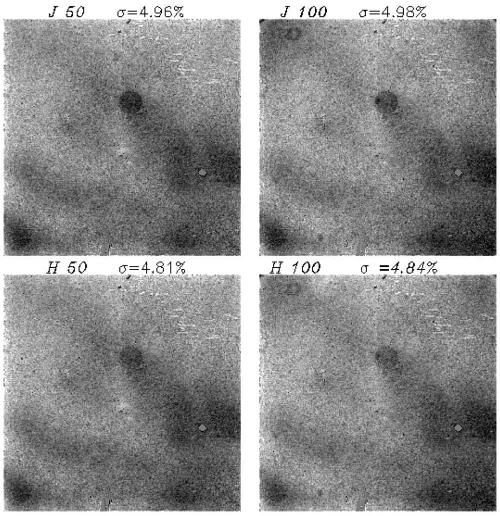

Figure 2: Pixel response map of SHARPII+ for J, H, SK, K band with the 100mas/pixel scale. Standard deviation is less than 5%. The central dark spot corresponds to pixels that were under the coronographic mask. Those pixels were under-exposed for a few hours and gave a lower response. Note that this effect is evolving from one band to another: it simply disappears with time.

- The pixel response map should be derived from daylight sky data with a signal in the raw frames higher than 4 000 ADU (RON$\sim$4 ADU). We observe spatial structures and higher standard deviation in the pixel response map derived from the integrating sphere flat-field.
- The pixel response map is modulated by the ADONIS optics transmission along the light path. When observing faint extended sources, the pixel response map should be derived for every "ON/OFF" positions.

- The pixel response map can be locally affected by remanence effects like any NICMOS3 detector. One should avoid to over-expose or under-expose parts of the detector before recording skylight frames. It gives rise to inhomogeneous response over the detector (see figure 2).

In the 3-5μm range, the background intensity is function of airmass value at a first order. The pixel response map is derived from data cube at various airmass for the given "ON/OFF" positions. Standard deviation over the pixel response map is ~8% and ~10% respectively in L band and M band.

3.2.3 PSF variations

Under bad seeing conditions ($\leq 1.5''$, $\tau_0 < 60$ms), atmospheric turbulence characteristics changes induce different response of the AO system, leading to PSF characteristics variations: higher centroid position variation, higher FWHM and Strehl ratio variation and higher speckle noise. The time-scale of those variations has to be taken into account when choosing the integration time. The larger the integration, the higher the loss in resolution, SR, and the lower the detectivity in the halo of bright sources. To illustrate that matter, we present in figure 3 a set of bad data (seeing $\sim 1.5''$) taken on AG Carinae (m_V=7.0) in december 96. We recorded 120 frames of 300 ms individual integration time in the SK band. The SR are ranging between 6% and 31%, the FWHM values from $0.14''$ to $0.28''$ and the standard deviation of the centroid position are of the order of the pixel size.

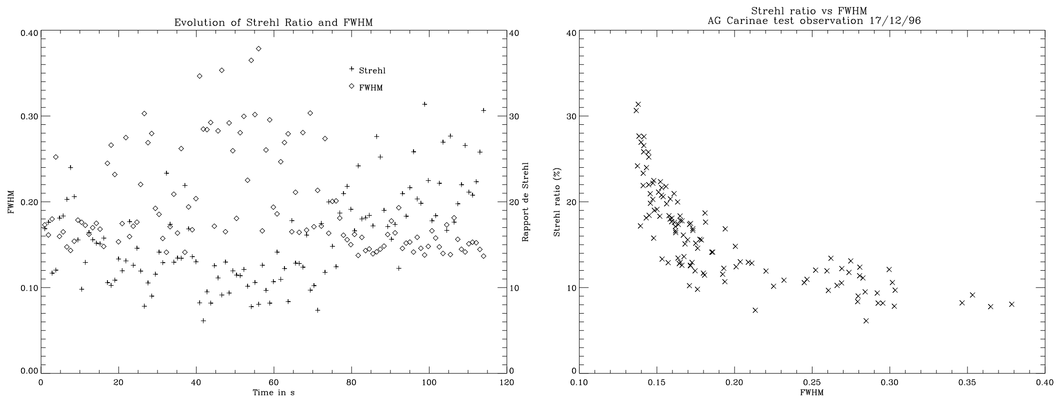

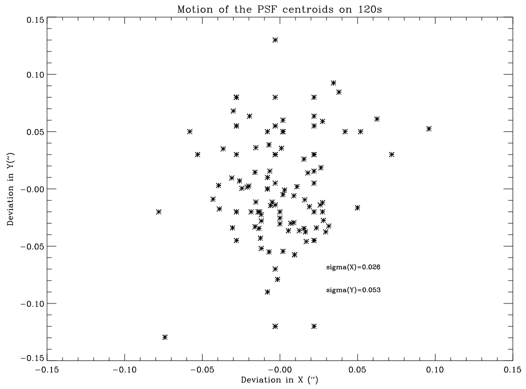

Figure 3: AG Carinae point spread function characteristics variations under bad seeing conditions ($\sim 1.5''$) in SK band with SHARPII+. **Upper Left:** FWHM values and Strehl ratio for the star versus time. **Upper Right:** FWHM versus Strehl ratio. **Left:** X and Y centroid variations. Standard deviation in X and Y are respectively $0.026''$ and $0.053''$.

For this bad set of data, we have sorted the FWHM and SR values and computed the average over the 4 best frames, and over the entire set (which would be the result if one integrates longer). We display in figure 4 the resulting frames and the PSF profiles. The averaged frame over the entire set show a loss of resolution 30% with respect to the best average and the halo intensity at the first diffraction ring position shows a value 8% higher than the best average.
The FWHM values dispersion is a well known effect for stars with SR below 15%. Going to shorter the wavelength, the PSF variations appear even stronger. During the observations under medium or bad seeing conditions, the observer will have to fit the individual integration time with the PSF stability timescale. The astronomer can best

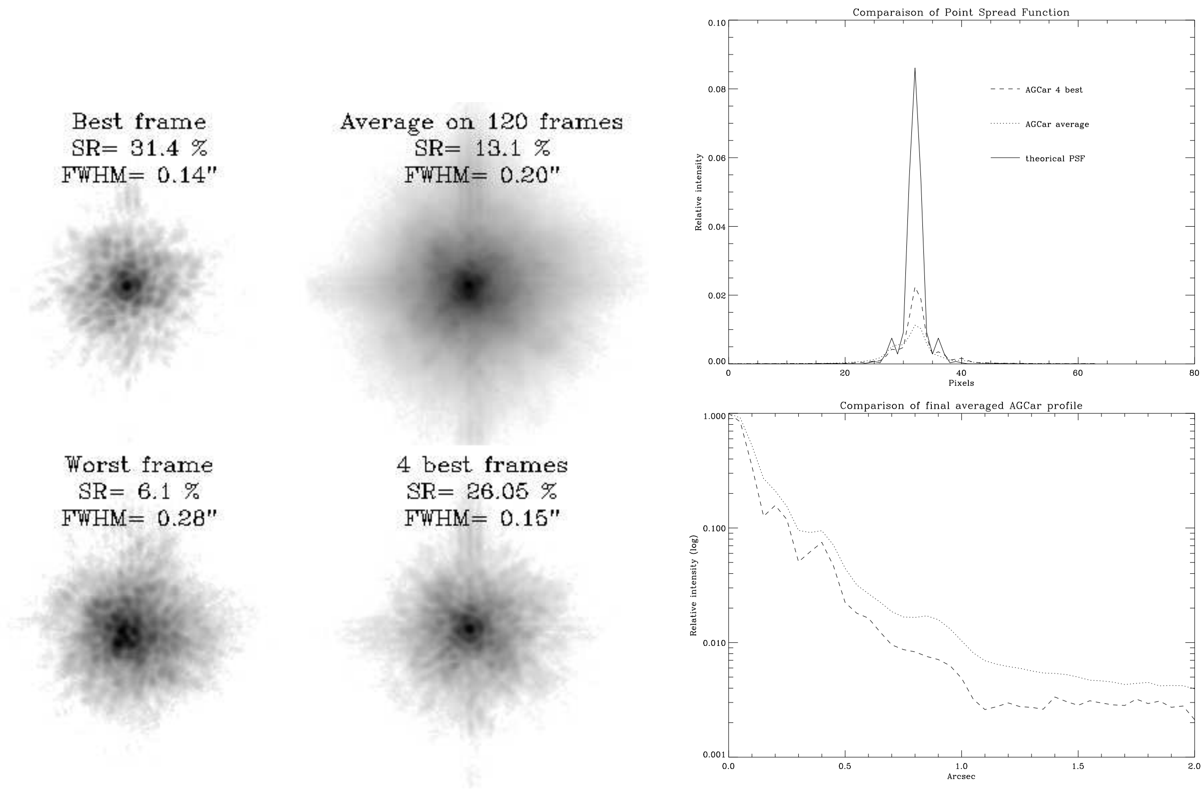

Figure 4: Illustration of the PSF shape variations between the best and worst case. **Left:** Individual and average images for AGCarinae. **Upper Right panel:** profiles for theorical PSF, entire set average and 4 best frames average. The peak to peak ratio corresponds to the SR. **Bottom right panel:** Comparison of normalized profile of two average frames (see text)

optimize his observations by following-up the correction efficiency and variations given by the *Performance Estimator* tool on the ADONIS workstation.

3.3 Consequence on observing strategy

It appears that the image quality is limited by various parameters that do not follow the same behavior.
In J band, the background photon flux and noise is negligible over time-scale of 1 min, but the PSF is highly variable due to partial AO correction in this band.
In K band we see the opposite effect where the PSF is much more stable, but the background emission is higher and induces shorter time sequences.
In L and M band, the SR might be as high as 60%-70% leading to a very stable PSF. On the other hand, the integration time cannot be larger than t_{BLIP} due to background variation on very short time-scale.

The atmospheric characteristics (seeing, correlation time, AO efficiency, humidity, airmass, wind speed, ..) are traced with various tools at the La Silla observatory, it is then possible for the observer to adapt his observing parameters and priorities given those numbers.

3.4 A tutorial case: observing Io using COMIC camera

3.4.1 Introduction: Observation of a planetary object

Io, the innermost satellite of Jupiter, is the source of a volcanic activity which was first observed during the Voyager encounter in 1979 (Pearl et al. 1982). This volcanism is detected as hot spots with temperatures approaching 700K. New hot spots were observed by Galileo with temperatures as high as 1500K (Lopes-Gauthier et al. 1997). This activity is temporally and spatially variable. In NIR wavelength the solar reflection is negligible compared to the 700K thermal emission on the satellite.
In general, observations of planetary objects are the least dependent on the sensitivity limit of the adaptive optics system. Indeed, solar system objects reflect part of the solar flux and they are bright enough at visible wavelength to be used as reference for the wavefront analysis.
Solar system objects have their own motion with respect to the stars. To avoid any effect of smearing which would blur the image, one usually uses the differential guiding of the telescope. In the case of adaptive optics systems, the tip-tilt compensation of the system can be used to follow the object. In this case, the telescope is moved when one reaches the linearity limit of the tip-tilt mirror, i.e. $5''$ for the ADONIS system. For Io, at $\sim$3 R_J of Jupiter's center (projected on the sky), observation can be performed during 10 min without moving the telescope.
Io's brightness ($m_V \sim 5$ and angular size $\sim 1''$) allow wavefront analysis using the RETICON sensor on the object itself.
The effect of diffused light from Jupiter is negligible beyond $5''$ from the planet limb. This value is highly dependent on seeing conditions and on relative planet and satellite brightnesses. The effect of diffuse light can be partly corrected by subtraction of a background frame previously recorded at the same distance of the planet. Even if some peculiarities exist, the observations of a satellite like Io is one of the simplest planetary observations which can be done with ADONIS. Other kind of observations based upon some special events, as Io in eclipse observed with another galilean satellites, Saturn ring during a 'passage of star', aurorae of Jupiter with a galilean satellites as reference, and others, needs efficient coordination of telescope team to successfully get good science and sometimes unique data.

3.4.2 Observations and data reduction

Io is locked into the gravity field of Jupiter and thus, its 40.7 hour orbital period is also its rotation period. Two data sets have been taken during two consecutive nights and corresponds to observations of both sides of Io.
Io was observed by one of us (FM) on October 21^{st} and 22^{nd}, 1996 using the COMIC camera, in L' band

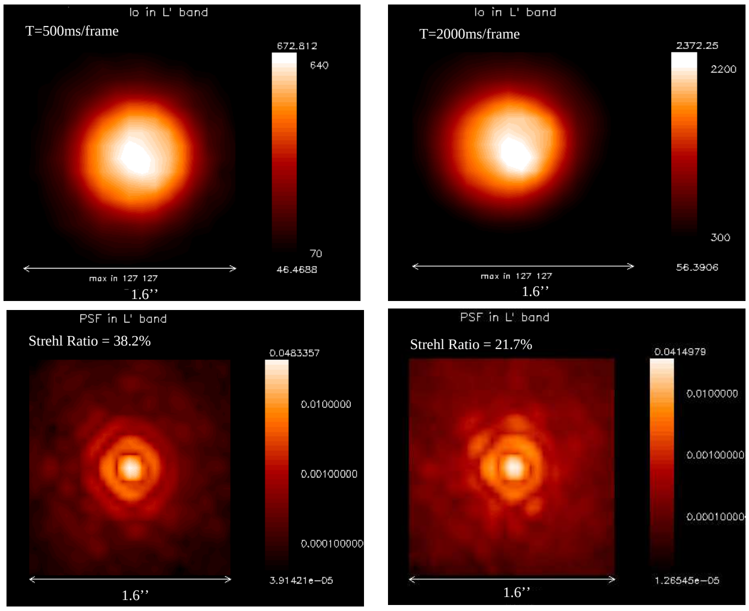

Figure 5: Final reduced images of Io and its PSF calibrator star for both nights. Io is clearly resolved, bright structures on Io appear to be different in the two data sets. The Strehl ratio of the PSFs are 21.7% for the first night and 38.2% for the second. Both final images clearly show the first Airy ring composed by fix pattern (trefoil) and an extended halo due to residual wavefront errors.

($\lambda = 3.809 \pm 0.623\mu$m) with the $0.100''$/pixel scale. The diffraction limit of the 3.6m telescope at this wavelength is $0.22''$. Seeing, measured by the La Silla DIMM telescope was 0.7-0.8$''$. The sub-earth points (SEP) coordinates were $\omega = +131.86, \delta = -1.618$ and $\omega = +320.54, \delta = -1.613$ respectively. A cube of data consists on 16 frames of 1s integration time each. The sky background was recorded using the "ON/OFF". The signal to noise ratio in the raw frames is 150 on the objet. We did not correct for instrumental inhomogeneities since the procedure is time consuming and since those background features intensity are negligible compared to the object brightness. A PSF calibrator star HD174974 (mv=5.0, spectral type G5) with similar brightness and close enough to the satellite (less than 2°) was also observed.

Basic processing of the data (sky subtraction, flat field correction and bad pixel removal) was done using ESO infrared data reduction software **eclipse** (*http://www.eso.org/eclipse*). Pixel response map was derived from a set of sky exposures taken at different air-masses with the same integration time.
The same data reduction procedure was applied on both the Io images and its PSF calibrator images. The resulting images are shown in figure 5. The S/N of the PSF calibrator stars are very high, so the application of a deconvolution method is expected to be efficient in sharpening the object image.

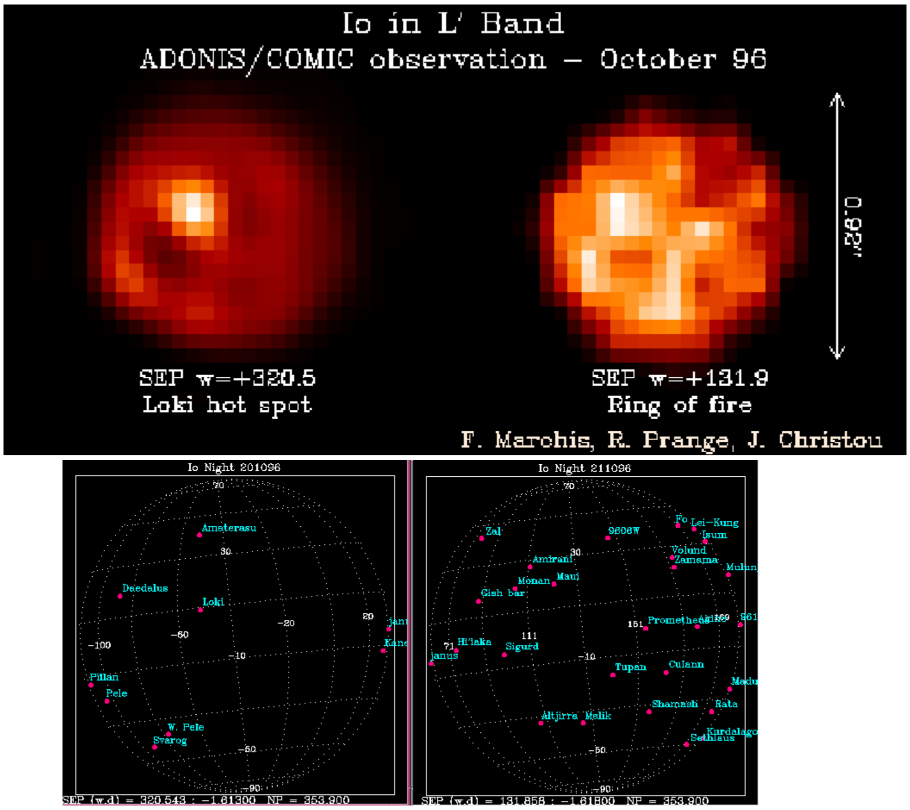

Figure 6: IDAC deconvolved images of both sides of Io compared to Galileo observations (see text).

We used various well-known deconvolution methods, such as Wiener filtering, Lucy-Richardson and maximum entropy methods. In such cases, the cube was compiled into a single frame by a shift-and-add method. The single Io mean frame obtained was deconvolved by the single PSF mean frame. Results were satisfactory for the main bright features. Using a different PSF taken a few minutes later, we noticed a variation of the faintest features on the disk. The correlation coefficient, calculated only on the satellite disk, for a given image deconvolved using two different PSFs is around 0.85. In fact, the PSF image obtained, observing a close star is a way to get an approximation of the PSF of the system. The PSF, in that case, was observed a few minutes after the object and located at 2° from the object, so that turbulence is expected to be slightly different between object and PSF. Moreover, we observe PSF characteristics variations from frame to frame in every data cube. Those variations are coming from the AO correction residuals variation due to the variability of the atmospheric turbulence. As an example, on October 22^{nd} the Strehl ratio of 40 images taken over 1 min was 35% ± 10%.

As a solution to this problem, a myopic deconvolution method called IDAC, has been initially developed by S. Jefferies and J. Christou (Jefferie et al. 1993). IDAC permits recovery of the object distribution and its PSF simultaneously. It is based upon a conjugate gradient driven least-squares relaxation applied to multiple observations. IDAC has been extensively tested on ADONIS data. More information about tutorial cases can be found in previous articles (Christou et al. 1994 and 1998). After IDAC deconvolution, features on disk of Io are more stable and the correlation coefficient of one image deconvolved by different PSF is close to 0.95.

3.4.3 Discussion of the results, perspectives

The both sides of Io reveal remarkable differences, as shown in figure 6. On October 21, the sub-earth face is characterized by a predominant hot spot and two secondary groups near the south-west limb. The brightest source is obviously Loki which has already been detected from the ground . It is the most frequently observed hot spot because of its permanent brightness and its position on the Jupiter facing side which favors observation from the ground (in eclipse or occultation by photometry variation (Spencer et al. 1990)).
The brightest secondary spot is close to the position of Pillan-Pele (our resolution is not high enough to separate both volcanos). Amaterasu seems not to be active at present, and was never detected by Galileo on its first orbit. It might be classified as temporal hot spots which are generally located at higher latitude.
On the other satellite side, bright features are numerous and at a comparably low intensity. We compare our data to the Galileo/NIMS data (Rosaly et al. 1997) taken on the 6 first orbits of Galileo (the only instrument able to observed this face with good sensitivity an effective spatial resolution). Our present result was confirmed by these Galileo observations which detected 26 hot spots on this side during its first orbits. The main feature called "ring of fire" is composed by the brightest hot spots. Comparing the image to the Galileo data, we conclude that the following clusters of hot spots were active, Maui-Monan, Sigurd, Malik, Prometheus and probably Tupan. Fainter variations may be due to albedo variation on the surface of compositional origin.
At the present time, the ADONIS system is the only AO system equipped with 3-5μm range camera suitable to high angular resolution imaging of Io. Thus, we expect to carry out further observations of the Io volcanism before the end of Galileo mission. Such a follow up of hot spot activity and comparison with other ground-based or space satellite data at other wavelength will provide with better constraints (hot spot spatial distribution, temperature and time variability) on the modeling of Io volcanism.

4 Spectro-imaging and coronography with ADONIS:

4.1 Coronography

The imaging capabilities in the vicinity of bright sources are limited by the read-out noise and the linear capacity of the SHARPII+ detector. Increasing to saturation the central star flux would damage the SHARPII+ detector array. One way to reduce the contribution of read-out noise in the final image, and better detect sources showing high intensity contrast with the central star, is to make use of a coronograph. The ADONIS coronograph was built under ESO contract by Observatoire de Grenoble. It includes a set of focal mask ranging in diameter size from 0.35″ to 6″ and a Lyot stop in the following pupil plane. The ADONIS coronograph is extensively presented elsewhere in these proceedings (Beuzit et al. 1998).

4.2 Spectro-imaging capabilities

Narrow band imaging capabilities are offered at a resolution of ~ 140 for both cameras. Different field of astrophysics would benefit from higher spectral resolution combined to high angular resolution. Spectro-imaging of broad-line emission regions such as AGNs, or high velocities ejected nebulae gives information on the velocity field over those regions. Moreover, higher spectral resolution imaging on the narrow line emission region and a near continuum, would result in a better contrast between line and continuum intensity measurements.

The prefocal optics set of ADONIS includes two *Queensgate Instruments Ltd* Fabry-Perot etalons and their control electronics, provided under ESO contract by the MPIE Garching. The two FP offer a resolution of 1000 and 2200 corresponding to velocity values of respectively about 300km/s and 150km/s. For both FP, the wavelength domain is restricted to K band for a finesse value of about 40. Transmission value are of 0.85 and 0.65 respectively for FP1000 and FP2200.
Two observing methods are currently used with the FP etalon, either line to continuum measurements, or velocity field measurements by FP scanning through a broad emission line.

4.2.1 FP calibrations

The given etalon is manually installed for the night in the F/45 converging beam near the focal plane. It has then to be calibrated for:
- x, y parallelism to reduce the wavelength band-path variations across the field
- z spacing to adjust the central wavelength value
- transmission response for the science FP settings on a white source

An integrating sphere placed in the adaptive optics bench provide with a flat field illumination over the NIR array. The first two steps of the calibrations are done using a neon spectral lamp installed in the integrating sphere and we switch to a white lamp for the last calibration step.

Since they are slight variations of wavelength band-path across the field, we derive the wavelength shift for every pixel. This is done by scanning through the neon spectral line and provide with the phase map of the FP and its resolution value (see figure 7). The measured wavelength variation across the field is less than $\frac{FWHM}{10}$ for FP2200 and less than $\frac{FWHM}{4}$ for FP1000.

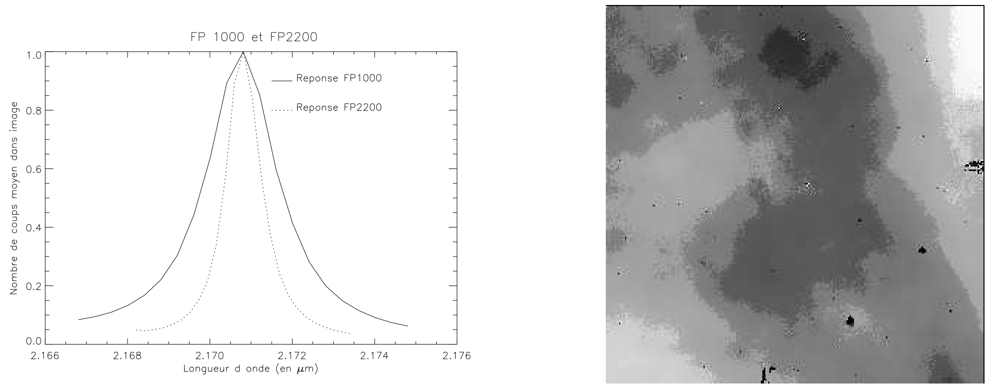

Figure 7: **Left:** Mean resolving power of FP1000 and FP2200 across the field for the 2.1708μm neon line. **Right:** Phase map for FP2200 with the 50mas/pixel scale (see text).

4.2.2 Calibration of the observations

The necessary calibration for the observations are:
- the pixel response map including all telescope, instrument and prefocal optics, for every observed wavelength
- the spectro-photometry calibration on a featureless star. That calibration includes the atmospheric and FP transmission for every wavelength.
- a PSF calibrator star for every observed wavelength

Quasi-monochromatic light as given by the FP wavelength band-path induces fringes on the NICMOS3 array. Those interferences might be generated within the sapphire substrate layer on the back side of the HgCdTe material (see Chalabaev et al., these proceedings). As seen on figure 8, there is a modulation of the pixel response across the field induced by the fringing. The variation is 15% peak to peak. The fringe pattern is shifted across the field from one

wavelength to an other and the modulation period as a function of wavelength is 3.3 nm.
To best correct for this modulation, careful flat-field have to be recorded during day time on the sky. Slight residual shift in the modulation might be found between the science frame and the pixel response map and would have to be corrected.
The spectro-photometric calibrations should be observed to calibrate the flux and correct for the atmospheric transmission. Apart of the very strong atmospheric absorption between 2.05μm and 2.08μm the K band has a rather flat transmission at a resolution of 1100 (Mc Gregor 1997). We compare in figure 8 the transmission curve from Mc Gregor to our measurements for the 2.04-2.08μm spectral region and found a good agreement for the atmospheric transmission.

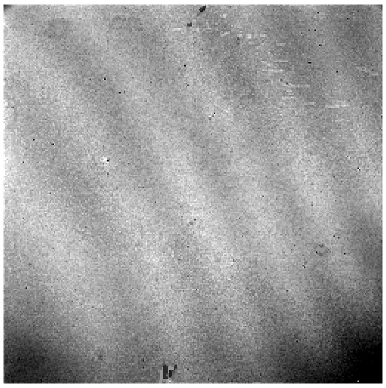

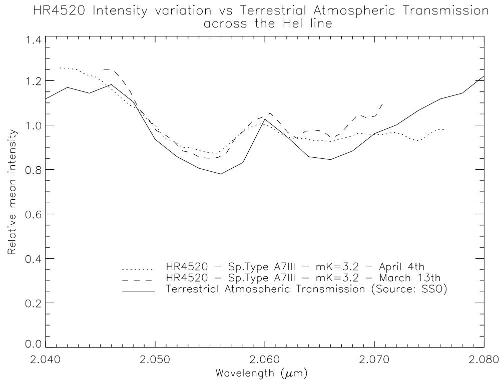

Figure 8: **Left:** Pixel response map derived from sky light data. The modulation of the response by the fringing of the FP induces peak to peak variation of 10%. **Right:**The strong absorption feature at 2.04-2.08μm: Atmospheric transmission curve at a resolution of 1100 as measured at Siding Spring Observatory (Mc Gregor 1997) compared to our spectro-photometric calibration with the Fabry-Perot etalon of resolution 1000

4.2.3 Observational methods

As already said, line to continuum measurements and FP scanning through the line are the two different observing mode.
The line to continuum mode using a Fabry-Perot allows to adjust precisely the emission wavelength value accounting for redshift or any proper velocity shift. The continuum value can be adjusted as a function of the emission line width. This method provide higher contrast between line and continuum than narrow band filter and has been used to image molecular hydrogen towards the TTauri prototype star (Quirrenbach & Zinnecker 1997).
The scanning method is a powerful way to derive the properties velocity field of the emission region. The spectral interval to scan and the number of FP positioning steps can be chosen as a function of the emission line. The spectrum along the FP scan data cube can be extracted for every pixel, giving for any part of the emitting region the peak intensity and wavelength, and, the line profile and width.
Still one has to pay attention because that method might be also a time consuming one that can be easily affected by external variations. The FP scan element resolution might be chosen as $\frac{FWHM}{2}$, so that an entire scan of a broad emission line region would result in about 40 FP positioning steps. As individual integration time of 1 min are something usual when observing a relatively faint source with a FP etalon, the entire FP scan can last as long as 40 to 60 min. In such a case, the spatial PSF might have changed across the scan, and it might be meaningless to record a PSF calibrator star. The spectro-photometry variations might be no longer negligible and this would give rise of incertitudes in the velocity map.

4.3 Combining coronography and Fabry-Perot:

During a test period, we investigated the possibility to combine coronography and spectro-imaging capabilities. This original method can be applied to velocity field measurements in broad-line emission regions around bright object.

For that purpose, we observed η Carinae through the helium line emission at 2.0581μm. η Carinae is an evolved super massive star, classified as an extreme Luminous Blue Variable star. η Carinae has expelled its upper layers in a great eruption in the 19^{th} century. It is now surrounded by a $12'' \times 18''$nebula composed of dust and gaz, mainly emitting in scattered light from the central source.
In order to have sufficient room to install both FP1000 etalon and coronograph mounts, we had to move the etalon 10 cm away from its nominal position. This displacement did not have any consequence on the wavelength band-path variation across the field. Using the 100mas/pixel scale, we observe a reflection of the coronographic mask on the array. By adjusting the "ON/OFF" mirror and the coronographic mask on the field of view, this reflection can be moved to the border of the field.
The coronographic mask size that we used was $4''$ in diameter. The resolution in the image (cf figure 9) measured on the nearby faint star is about $0.2''$. The structure on the nebula is clearly defined, and one can easily distinguish the

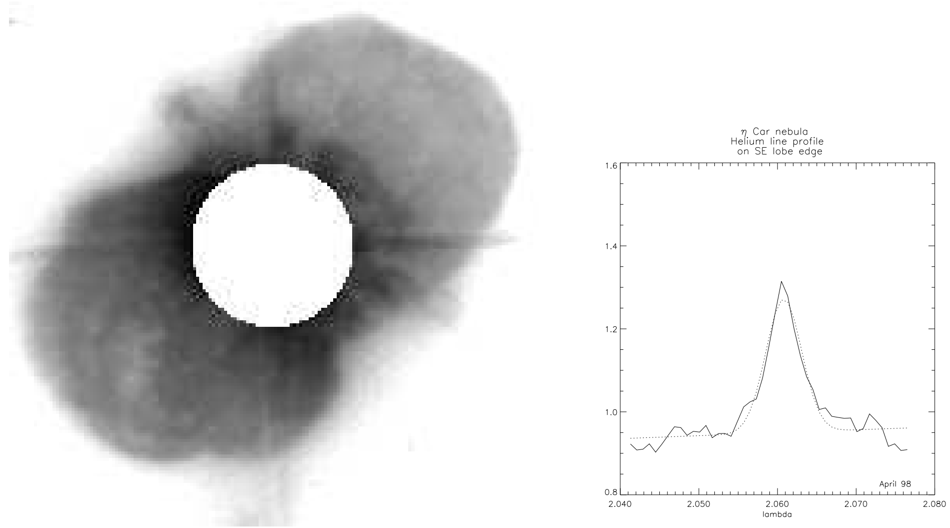

Figure 9: η Carinae observed during a test night with a method combining the coronograph and the Fabry-Perot etalon. North is up, East to the left. The field of view is $17'' \times 17''$

SE and NW lobes and the equatorial material of the nebula. We have corrected for the atmospheric transmission, but due to the strong atmospheric absorption feature at that wavelength, precise spectrum analysis might be quite cumbersome. Just to illustrate the concept of spectrum along the data cube, we plot the SE and NW lobe edges spectra (see figure 9).

5 Conclusive remarks

Adaptive optics can be advantageously coupled with different observing mode as we have shown. Recently, the Grenoble/GraF instrument has been successfully tested with ADONIS. This instrument offer integral field and long slit spectroscopy (see Chalabaev et al., these proceedings). In the near future, a near infrared wavefront sensor will be installed and tested on ADONIS. All those different complementary instruments of an adaptive optics system extend the observational fields and the output science of AO systems.

Bibliography:

- Beuzit, J.-L., Demailly, L. ,Gendron, E., Gigan, P. , Lacombe, F., Rouan, D., Hubin, N., Bonaccini, D. , Prieto, E., Chazallet, F., Rabaud, D., Madec, P.-Y. , Rousset, G., Hofmann, R., Eisenhauer, F. 1997,, *Adaptive Optics on a 3.6-Meter Telescope. The ADONIS System.*, Experimental Astronomy, **7**, 285–292

- Beuzit, J.L., Mouillet, D., Le Mignant, D., ?? , "The ADONIS coronograph", these proceedings

- Bonaccini, D., Prieto, E., Corporon, P., Christou, J., Le Mignant, D., Prado, P., & Hubin, N. 1997, *The performances of the ESO/AO system* ADONIS *at La Silla 3.6m telescope*, Paper#3126-78, SPIE, San Diego
- Chalabaev, A., le Coarer, E., Rabou, P., Magnard, Y., Petmezakis, P., & Le Mignant, D., *GraF intergral field and long slit spectroscopy with the ESO 3.6m/*ADONIS/SHARPII+ *system*, these proceedings
- Gendron, E. & Lena, P. 1995, *Astronomical adaptive optics. II. Experimental results of an optimized modal control.*, A&ASpS, **111**, 153
- Christou J.C., E.K. Hege, S.M. Jefferies & C.U. Keller 1994, Proc SPIE, **2200**, 433-444
- Christou J.C., F. Marchis, N. Ageorge, D. Bonaccini & F. Rigaut 1998, SPIE, Kona (Hawaii)
- Christou J.C., D. Bonaccini, N. Ageorge, O. Von der Luhe, Deconvolution of Adaptative Optics near-infrared system (ADONIS) images 1997, SPIE, **3126**, 589-594
- Devillard, N. 1997, *The ESO* **eclipse** *data reduction package*, The Messenger, **87**, 19
- Eisenhauer, F. & Hofmann, R. 1996, *SharpII user manual - ESO Doc NoGEN-MAN-MPE-11620-0007*
- Geoffray, H., *Thermal baqckground blurrin by* ADONIS, These proceedings
- Jefferies S.M., J.C. Christou 1993, Ap.J., **415**, 862
- Lacombe, F., Marco, O., Geoffray, H., Beuzit, J. L. , Monin, J. L., Gigan, P., Talureau, B., Feautrier, P. , Petmezakis, P., Bonaccini, D. 19998, *Adaptive Optics Imaging at 1-5 Microns on Large Telescopes:The COMIC Camera for ADONIS*, PASP, **110**, 1087–1097
- Le Mignant, D., Gendron, E. & Marchis F., *The ESO/*ADONIS *AO system: Study of the 3-5μm background emissivity*, these proceedings
- Lopes-Gautier R.,A.G. Davies, R. Carlson, W. Smythe, L. Kamp, L. Soderblom, F.E. Leader, R. Mehlman & Galileo team 1997, Geophys. Res. Lett., **24**, 2439-2442
- Mc Gregor, P. 1997, *Users Manual of CASPIR*, Siding Spring Observatory
- Quirrenbach, A., & Zinnecker, H. 1997, *Molecular hydrogen towards T Tauri observed with adaptive optics*, The Messenger, **87**, 36–39
- Spencer J., M.A. Shure, M.E. Ressler, J.D. Goguen, W.M. Sinton, D.W. Toomey, A. Denault & J. Westfall 1990, Discovery of hotspots on Io using disk-resolved infrared imaging, Nature, , **348**, 618